Multiple scattering approach for two-electron resonant emission studied by angle-resolved coincidence spectroscopy

F. Da Pieve,[1,2] D. Sébilleau,[3] S. Di Matteo,[3] R. Gunnella,[4] R. Gotter,[5] A. Ruocco,[2] G. Stefani,[2] and C. R. Natoli[6]

[1]*Institut Carnot de Bourgogne, UMR 5209 CNRS-Université de Bourgogne, BP 47870, 21078 Dijon Cedex, France*

[2]*Dipartimento di Fisica, Università Roma Tre and CNISM, via della Vasca Navale 84, I-00146 Rome, Italy*

[3]*Équipe de Physique des Surfaces et des Interfaces, Institut de Physique de Rennes, UMR CNRS-UR1 6251, Université de Rennes 1, 35042 Rennes Cédex, France*

[4]*Dipartimento di Fisica, Università di Camerino, Via Madonna delle Carceri, I-62032 Camerino, Italy*

[5]*Laboratorio Nazionale TASC-INFM-CNR, AREA Science Park, SS 14 Km 163, 5 I-34012 Basovizza, Trieste, Italy*

[6]*Laboratori Nazionali di Frascati, INFN, via E. Fermi 40, I-00044 Frascati, Italy*

(Received 21 April 2008; published 22 July 2008)

We have developed a generalization of the multiple-scattering formalism to deal with Auger-photoelectron coincidence spectroscopy (APECS) in the solid state. We have merged the exact atomic treatment of the angular correlations between the two electrons and the single-particle approach, on which the multiple-scattering description of condensed matter relies. This allows the recovering, even in extended systems, of the entangled form of the electron-pair wave function characterizing the coincidence angular diffraction pattern. In the atomic limit our formalism correctly reproduces the cross section, as calculated within the statistical-tensors approach, usually employed in atomic physics. We have then performed numerical calculations for the Ge(100) $L_3M_{45}M_{45}$ APECS and compared the results with previous experiments. We found that, in the given geometry, the diffraction patterns in coincidence with different directions of the photoelectron keep little memory of the atomic anisotropy. We speculate on the conditions to be fulfilled in order to enhance the atomic-orbital sensitivity in APECS through solid-state diffraction effects.

DOI: 10.1103/PhysRevB.78.035122 PACS number(s): 79.60.Bm

I. INTRODUCTION

Auger-photoelectron coincidence spectroscopy (APECS) has proved to be a very powerful tool in studying electronic correlations.[1] In fact, whereas conventional Auger spectroscopy is often unable to resolve the overlapping features due to different core holes or if it contains multiplet structure, APECS allows measurement of the individual line shapes and the singling out of each component of the spectrum. In atomic physics, the coincidence technique has a long tradition and theory has given great support to experimentalists: the coincidence cross section is derived within the statistical-tensors formalism,[2,3] which allows for a many-body treatment of rotationally invariant problems. The two electrons that are detected in time coincidence are considered as emitted from ionization and decay of the same selected core hole. The nonisotropic distribution of the Auger electron is determined by the alignment or orientation of the intermediate ion, i.e., a nonstatistical distribution of the orbital sublevels in the intermediate state. Such a nonstatistical distribution is determined by both the direction of polarization of the incident photon beam and the detection angles of the photoelectron. This in turn fixes both the shape and the symmetry of the Auger coincidence distribution, as shown, e.g., in Refs. 4 and 5 The difference between the conventional single-particle and coincidence angular distributions can be considered as an evidence of the entanglement of the two-electron state. In atomic physics, the study of coincidence angular distributions, together with coincidence energy spectra, offers the opportunity to investigate interference and postcollision effects, whose exploration is a topic of strong current interest.[6]

In the past decade, there has been a growing interest for APECS experiments in the context of condensed-matter physics, where, besides the previously outlined features, APECS is also characterized by an enhanced surface sensitivity,[7] and was used to resolve the energy shift of surface and bulk core-level peaks[8] or to perform emission depth selectivity studies.[9,10] In the present paper we shall focus on angular-resolved APECS (AR-APECS) experiments in the solid state,[11] performed with the aim of investigating orbital and electronic correlations in extended systems. The authors of Ref. 11 studied the Ge(100) $L_3M_{45}M_{45}$ Auger angular distributions in coincidence with different directions of the photoelectron. They found clear differences between single and coincidence Auger diffraction patterns as well as a shift of the coincidence-peak positions, depending on the specific detection angles of the photoelectron. Such findings were explained in terms of a different degree of alignment in the intermediate state, determined by the direction of the photoelectron detection, similarly to what is usually done in atomic physics. The authors therefore argued that the diffraction process does not destroy the information contained in the coincidence atomic distribution. This interpretation has given strength to the idea that the atomic anisotropy might play an important role in determining both the final angular distribution and the energy spectrum in condensed matter as well.

It is interesting to note that, in this framework, it is the detection of the photoelectron at a certain angle that makes the Auger electron fall in a well-determined state, which is the idea at the basis of the concept of entanglement. Indeed, if this were the case, the difference between the conventional single-particle and coincidence angular distributions could be considered as a measure of the nonseparability of the two electrons. However, as indicated by the authors themselves, the conclusions of Ref. 11 needed deeper theoretical support

than the qualitative arguments advanced therein in order to clarify the origin of the observed effects and to demonstrate that the initial atomic correlations between the two electrons survive the diffraction effects of extended systems. Unfortunately, the statistical-tensor formalism of atomic physics,[2,3] which is based on the rotational invariance of the system, cannot be translated to this case as the rotational invariance is broken in solids.

We have therefore developed in this paper an extension of the multiple-scattering approach presented in Ref. 4 to treat two-electron angular coincidence spectroscopy in condensed matter. To achieve this, we have considered the exact angular correlation between the two electrons at the emitting atomic site and then allow them to diffract in the crystal as independent particles. Therefore the origin of the angular correlations of the Auger electron and the photoelectron purely resides in the transition selection rules that impose the Auger decay to fill in the orbital level whose quantum numbers characterize also the state of the emitted photoelectron. In the atomic limit, our cross section reduces to a tensor formulation, which is equivalent to the one derived within the statistical-tensor approach. This limit describes well the coincidence data from $L_3M_{23}M_{23}$ of atomic Ar, as shown in Ref. 4. In the present work we perform numerical calculations for both conventional and coincidence Auger patterns in the case of Ge(100) $L_3M_{45}M_{45}$ Auger decay, and compare them with the experimental data of Ref. 11.

The paper is organized as follows: in Sec. II we review the fundamental principles of the multiple-scattering theory. In Sec. III we deduce the coincidence cross section for two correlated electrons emitted from a solid sample and in Sec. IV we derive its atomic limit. Section V is devoted to the details of the numerical calculations, whereas the results for conventional Auger diffraction and coincidence diffraction patterns in different geometrical conditions is described in Sec. VI. In Sec. VII we draw our conclusions.

II. FUNDAMENTALS OF MULTIPLE SCATTERING THEORY

Multiple scattering (MS) is used for the interpretation of several kinds of spectroscopies.[12] In this approach, the solution of the Schrödinger equation for a cluster of atoms is derived in two steps: we first solve the equation within the cells around each site and then match the solutions at the boundaries of the various cells. The delocalization of the electronic wave function is determined as the result of repeated scattering processes of the electron by the atomic sites. The MS approach relies on an effective one-electron theory: the excited electron, as it traverses the solid, behaves as a quasiparticle that moves in an effective complex-valued optical potential. Correlation effects are taken into account in an average way in the framework of the local-density scheme through the introduction of an exchange-correlation potential.[13]

The task is to solve the Schrödinger equation,

$$[\nabla^2 + k^2 - V(\mathbf{r})]\psi_k^+(\mathbf{r}) = 0, \tag{1}$$

with the appropriate boundary conditions. The potential in Eq. (1) is given by $V(\mathbf{r}) = V_c + V_{xc} + V_c + \Sigma$, where V_c is the Coulomb potential and V_{xc} denotes the exchange-correlation potential, which can be approximated with an energy dependent self-energy Σ. For continuum states, Eq. (1) is supplemented by the scattering wave boundary conditions:

$$\psi_k^+(\mathbf{r})_{r\to\infty} \simeq e^{+i\mathbf{k}\cdot\mathbf{r}} - f(\mathbf{k},\mathbf{r})\frac{e^{ikr}}{r}, \tag{2}$$

which represents an incident plane wave traveling in the direction $\mathbf{k}$ and an outgoing scattered spherical wave. The essence of the MS theory rests on the partition of space into Voronoi polyhedra (equivalent to Wigner-Seitz cells for periodic systems) and on finding a local solution inside each volume. Then the overall solution is expanded in each cell using such local solutions. In the muffin-tin approximation, the solution inside the ith atomic muffin-tin sphere can be written as

$$\psi_{\mathbf{k}}(\mathbf{r}_i) = \frac{1}{4\pi}\sqrt{\frac{k}{\pi}}\sum_{lm\sigma} B^i_{lm}(\mathbf{k}) R_{\epsilon l}(r_i) Y^*_{lm}(\hat{\mathbf{r}}_i)\chi_\sigma, \tag{3}$$

where the $B^i_{lm}(\mathbf{k})$ are called scattering amplitudes and obey the MS equations:

$$\sum_j \sum_{lm} M^{ij}_{lm,l'm'} B^j_{l'm'}(\mathbf{k}) = i^l Y_{lm}(\hat{\mathbf{k}}) e^{i\mathbf{k}\cdot\mathbf{R}_i}. \tag{4}$$

Here $M^{ij}_{lm,l'm'}$ is the MS matrix:

$$M^{ij}_{lm,l'm'} = (t^{i^{-1}}_{lm,l'm'}\delta_{ll'}\delta_{mm'} + G^{ij}_{lm,l'm'}), \tag{5}$$

which is given in terms of the individual atomic scattering matrices, $t^{i^{-1}}_{lm,l'm'}\delta_{ll'}\delta_{mm'}$, and the free spherical wave propagator, $G^{ij}_{lm,l'm'}$, which describes the propagation of the electron from one site to the other. By introducing the scattering path operator $\tau^{ij}_{lm,l'm'}$ as the inverse of the MS matrix, the solution for the scattering amplitudes B^i_{lm} is obtained as

$$B^i_{lm} = \sum_j \sum_{l'm'} \tau^{ij}_{lm,l'm'} i^{l'} Y_{l'm'}(\hat{\mathbf{k}}) e^{i\mathbf{k}\cdot\mathbf{R}_{jo}}. \tag{6}$$

The scattering path operator $\tau^{ij}_{lm,l'm'}$ represents the probability amplitude for the excited electron to propagate from site i, with angular momentum l,m, to site j with angular momentum l',m'. $Y_{l'm'}(\hat{\mathbf{k}})$ represents the amplitude for emission along direction $\hat{\mathbf{k}}$ with angular momentum l',m', and the phase factor $e^{i\mathbf{k}\cdot\mathbf{R}_{jo}}$ takes into account the phase relation of the electronic wave between sites o (the origin of the coordinates) and j. For low kinetic energy of the emitted electron ($\leq$50 eV), MS effects are sizable and it is necessary to invert the whole MS matrix. In most cases, above $\simeq$50 eV, the scattering path operator can be calculated by series expansion, i.e.,

$$\tau = (T^{-1} + G)^{-1} = (I + TG)^{-1}T = T\sum_n (-1)^n (GT)^n, \tag{7}$$

where we have indicated the direct contribution $t^{i^{-1}}_{lm,l'm'}\delta_{ll'}\delta_{mm'}$ with T^{-1}. Thus the scattering path operator is expanded in terms of the different scattering orders. If $n=0$, only the direct signal contributes, which differs from the

purely atomic signal for the presence of surface-barrier effects. The term with $n=1$ corresponds to a single-scattering event, and so on. The development in Eq. (7) works well in the high-energy region where MS corrections are weaker and few scattering orders are usually sufficient to reach convergence. In the following, we shall make use of this approximation due to the value of the kinetic energy of the electrons involved in the considered transition (250 and 1139 eV for the photoelectron and the Auger electron, respectively).

III. MULTIPLE SCATTERING APPROACH TO AUGER-PHOTOELECTRON COINCIDENCE SPECTROSCOPY

The purpose of this section is to present the building blocks for the description of the photoelectron-Auger-electron emission process in solids. The initial state is described by the ground state of the system plus an incoming photon. The final state is treated in terms of two outgoing electrons, which propagate in the solid and a residual doubly charged ion. The competitive process of direct double photoemission is neglected. The matrix element governing the process is then given by

$$\langle f|T|i\rangle = \sum_n \int_0^\infty \frac{\langle f|V_c|n_\tau\rangle\langle n_\tau|D|i\rangle}{E - E_n + \frac{i\Gamma_n}{2}} d\tau, \tag{8}$$

where D is the dipole operator and V_c is the Coulomb operator. This transition amplitude takes into account resonances in the ionization continuum described by the intermediate states n_τ. The summation over n implies the sum over discrete quantum numbers while the integration over τ exhausts the whole ionization continua of the intermediate states. In the following, as the energies of the two outgoing electrons are different and excitation takes place far from the threshold, we neglect interference and PCI effects. We can then use a two-step approach for the description of the process. The first step consists of the excitation from the ground state of the system ψ_g by photon absorption to a specific intermediate state, whose width is Γ_r and whose energy is $E_r^+ + \epsilon_p$, where E_r^+ denotes the energy of the intermediate state and ϵ_p the energy of the photoelectron. Then this intermediate state decays into a final state with energy $E_\beta^{++} + \epsilon_a$, where E_β^{++} is the energy of the two-hole final state and ϵ_a is the energy of the Auger electron. The angular correlations of the two electrons in this approach arise only at the atomic level through the transition selection rules that impose the Auger decay to fill in the orbital level whose quantum numbers characterize also the state of the emitted photoelectron. This was detailed in Ref. 4, where this approach has proven to be able to give satisfactory results in describing coincidence angular distributions from atomic targets.

In the following the quantum numbers l_c and j_c label the core hole, l_1 and l_2 the final holes, and L, S, and J the residual ion. In the single-particle approach and using an electron picture, the initial state is given by the core state electron. This spin-orbit core state can be written as

$$\psi_c(\mathbf{r}) = R_{nl_c}(r) \sum_{m_c\sigma_c} C^{j_c j_{cz}}_{l_c m_c 1/2\sigma_c} Y_{l_c m_c}(\hat{\mathbf{r}}) \chi_{\sigma_c}, \tag{9}$$

where χ_{σ_c} are usual spin functions and $C^{j_c j_{cz}}_{l_c m_c 1/2\sigma_c}$ are the Clebsch-Gordan coefficients. Due to the localization of the initial core state $\psi_c(\mathbf{r})$ at site i, we only need the expression for the final-state wave function at site i, i.e., the continuum wave function for the photoelectron is given by the solution of the MS problem projected on site i:

$$\psi_{\mathbf{k}_p}(\mathbf{r}_i) = \frac{1}{4\pi}\sqrt{\frac{k_p}{\pi}} \sum_{l_p m_p \sigma_p} B^i_{l_p m_p}(\mathbf{k}_p) R_{\epsilon l_p}(r_i) Y^*_{l_p m_p}(\hat{\mathbf{r}}_i) \chi_{\sigma_p}. \tag{10}$$

The continuum wave functions are normalized to one state per Rydberg. The transition operator in the dipole approximation can be written as

$$\hat{\boldsymbol{\epsilon}} \cdot \mathbf{r} = \frac{4\pi}{3} r \sum_\mu Y^*_{1\mu}(\hat{\boldsymbol{\epsilon}}) Y_{1\mu}(\hat{\mathbf{r}}). \tag{11}$$

The dipole matrix elements are then given by

$$\left\langle \psi_p^- \middle| \boldsymbol{\epsilon}\cdot\mathbf{r} \middle| l_c \frac{1}{2} j_c j_{cz} \right\rangle = \frac{4\pi}{3}\frac{1}{4\pi}\sqrt{\frac{k_p}{\pi}} \sum_\mu \sum_{l_p m_p \sigma_p m_c} Y^*_{1\mu}(\hat{\boldsymbol{\epsilon}}) \times R(nl_c, El_p) C^{j_c j_{cz}}_{l_c m_c 1/2-\sigma_p} B^i_{l_p m_p}(\mathbf{k}_p) \times \sqrt{\frac{3}{4\pi}}\frac{\hat{l}_c}{\hat{l}_p} C^{l_p 0}_{l_c 010} C^{l_p m_p}_{l_c m_c 1\mu} (-1)^{\sigma_p - 1/2}, \tag{12}$$

where ψ_p^- is the time reversed state of the photoelectron state. The Clebsch-Gordan coefficients result from integration of the angular variables and $R(nl_c, El_p)$ is the radial dipole matrix element. We defined $\hat{l} \equiv \sqrt{2l+1}$. In the second step, the Auger-electron wave function is written as solution of the MS problem in the same way as for the photoelectron; the core hole state is characterized by the same quantum numbers j_c and j_{cz} of the first step, which determine the angular correlation of the emitted electrons. However, the hole is allowed to migrate through m_c and σ_c sublevels without changing its energy:

$$\left\langle \psi_a^-, l_c \frac{1}{2} j_c j_{cz} \right| = \frac{1}{4\pi}\sqrt{\frac{k_a}{\pi}} R_{nl_c}(r_2) \sum_{l_a m_a \bar{\sigma}_c \bar{m}_c} R_{El_a}(r_1) \times B^i_{l_a m_a}(\mathbf{k}_a) \chi^+_{-\sigma_a} (-1)^{\sigma_a - 1/2} \chi^+_{\bar{\sigma}_c} C^{j_c j_{cz}}_{l_c \bar{m}_c 1/2\bar{\sigma}_c} \times \sum_{L_{ac} M_{ac}} C^{L_{ac} M_{ac}}_{l_a m_a l_c \bar{m}_c} [Y^*_{l_a}(\hat{\mathbf{r}}_1) \otimes Y^*_{l_c}(\hat{\mathbf{r}}_2)]_{L_{ac} M_{ac}}, \tag{13}$$

where we have introduced the bipolar spherical harmonic $[Y^*_{l_a}(\hat{\mathbf{r}}_1) \otimes Y^*_{l_c}(\hat{\mathbf{r}}_2)]_{L_{ac} M_{ac}}$.[14] The two holes are considered as localized and coupled to a multiplet term $^{2S+1}L_J$,

$$\left|\left[\left(l_1\frac{1}{2}l_2\frac{1}{2}\right)LS\right]JJ_z\right\rangle = \frac{1}{\sqrt{2}}\sum_{MS_z} C^{JJ_z}_{LMSS_z}\sum_{\sigma_1\sigma_2}\{R_{n_1l_1}(r_1)R_{n_2l_2}(r_2)[Y_{l_1}(\hat{\mathbf{r}}_1)\otimes Y_{l_2}(\hat{\mathbf{r}}_2)]_{LM}C^{SS_z}_{\frac{1}{2}\sigma_1\frac{1}{2}\sigma_2}\chi_{\sigma_1}(1)\chi_{\sigma_2}(2)$$
$$+(-1)^{l_1+l_2-L-S}R_{n_1l_1}(r_2)R_{n_2l_2}(r_1)[Y_{l_2}(\hat{\mathbf{r}}_1)\otimes Y_{l_1}(\hat{\mathbf{r}}_2)]_{LM}C^{SS_z}_{1/2\sigma_2 1/2\sigma_1}\chi_{\sigma_1}(2)\chi_{\sigma_2}(1)\}. \quad (14)$$

Thus we can write the Auger matrix element as

$$\left\langle \psi_a^-, l_c\frac{1}{2}j_cj_{cz}\left|\frac{e^2}{|\mathbf{r}_1-\mathbf{r}_2|}\right|[(l_1l_2)LS]JJ_z\right\rangle$$
$$=\frac{e^2}{\sqrt{2}}\frac{1}{4\pi}\sqrt{\frac{k_a}{\pi}}l_1l_2(-1)^{l_c+L}\sum_{l_ak}(-1)^{l_1}\left[D^k_{n_1l_1n_2l_2,\epsilon l_an_cl_c}C^{l_a0}_{l_10k0}C^{l_c0}_{l_20k0}\begin{pmatrix} l_2 & l_c & k\\ l_a & l_1 & L\end{pmatrix}+(-1)^{-L-S}E^k_{n_2l_2n_1l_1,\epsilon l_an_cl_c}C^{l_a0}_{l_20k0}C^{l_c0}_{l_10k0}\begin{pmatrix} l_1 & l_c & k\\ l_a & l_2 & L\end{pmatrix}\right]$$
$$\times\sum_{m_a\bar{m}_c\bar{\sigma}_cMS_z}C^{JJ_z}_{LMSS_z}C^{j_cj_{cz}}_{l_c\bar{m}_c1/2\bar{\sigma}_c}C^{LM}_{l_am_al_c\bar{m}_c}C^{SS_z}_{1/2-\sigma_a1/2\bar{\sigma}_c}(-1)^{\sigma_a-1/2}B^i_{l_am_a}(\mathbf{k}_a), \quad (15)$$

where $D^k_{n_1l_1n_2l_2,\epsilon l_an_cl_c}$ and $E^k_{n_2l_2n_1l_1,\epsilon l_an_cl_c}$ are the direct and exchange radial integrals.

The intensity of the process can be written in terms of the scattering amplitudes as the following:

$$\frac{d^2\sigma}{d\mathbf{k}_ad\mathbf{k}_p}(l_c,j_c,l_1,l_2,L,S,J)=4\pi^2\alpha\hbar\omega\Gamma_L\sum_{\sigma_a\sigma_pJ_z}\left|\sum_{j_{c_z}}\left\langle\psi_a^-,l_c\frac{1}{2}j_cj_{cz}\left|\frac{e^2}{|\mathbf{r}_1-\mathbf{r}_2|}\right|((l_1l_2)LS)JJ_z\right\rangle\langle\psi_p^-|\boldsymbol{\epsilon}\cdot\mathbf{r}\left|l_c\frac{1}{2}j_cj_{cz}\right\rangle\right|^2$$
$$=\frac{e^4k_ak_p}{96\pi^3}\alpha\hbar\omega L_\Gamma|\hat{l}_1\hat{l}_2\hat{l}_c(-1)^{l_c+l_1+L}\sum_{l_pl_a\mu k}\frac{1}{\hat{l}_p}Y^*_{1\mu}(\hat{\boldsymbol{\epsilon}})R(n_cl_c,El_p)[D_k(n_1l_1n_2l_2,\epsilon l_an_cl_c)d_{kl_a}$$
$$+(-1)^{-L-S}E_k(n_2l_2n_1l_1,\epsilon l_an_cl_c)e_{kl_a}]\sum_{m_am_c\bar{m}_c\bar{\sigma}_cMS_z}C^{l_p0}_{l_c010}C^{l_pm_p}_{l_cm_c1\mu}C^{JJ_z}_{LMSS_z}C^{j_cj_{cz}}_{l_cm_c1/2-\sigma_p}$$
$$\times C^{j_cj_{cz}}_{l_c\bar{m}_c1/2\bar{\sigma}_c}C^{LM}_{l_am_al_c\bar{m}_c}C^{SS_z}_{1/2-\sigma_a1/2\bar{\sigma}_c}B^i_{l_am_a}(\mathbf{k}_a)B^i_{l_pm_p}(\mathbf{k}_p)\,(-1)^{1-\sigma_a-\sigma_p}|^2. \quad (16)$$

Here the factor L_Γ is proportional to a Lorentz function and comes from the denominator in Eq. (8) for a selected intermediate state. The labels σ_a, σ_p, and J_z represent, respectively, the spin projection of the Auger electron, the photoelectron, and the total momentum of the residual ion, which are not observed and therefore summed up. The sums over the projections of the intermediate state are internal, i.e., different m_l and σ_c sublevels contribute coherently to the intensity. The factors d_{kl_a}, e_{kl_a} result from integration over the angular variables in the Auger part and are given by

$$d_{kl_a}=C^{l_a0}_{l_10k0}C^{l_c0}_{l_20k0}\begin{Bmatrix} l_2 & l_c & k\\ l_a & l_1 & L\end{Bmatrix}, \quad (17)$$

and

$$e_{kl_a}=C^{l_a0}_{l_20k0}C^{l_c0}_{l_10k0}\begin{Bmatrix} l_1 & l_c & k\\ l_a & l_2 & L\end{Bmatrix}. \quad (18)$$

The first step in treating Eq. (16) is to eliminate the sums over dummy quantum numbers and then to recouple the remaining coefficients in order to build the bipolar scattering amplitudes, defined as

$$[B^i_{l_p}(\mathbf{k}_p)\otimes B^i_{l_a}(\mathbf{k}_a)]_{L_1M_1}=\sum_{m_pm_a}C^{L_1M_1}_{l_pm_pl_am_a}B^i_{l_pm_p}(\mathbf{k}_p)B^i_{l_am_a}(\mathbf{k}_a). \quad (19)$$

Recouplings are made in order to build also the radiation tensor, given by combination of spherical components of the polarization vector:

$$\rho^*_{L_0M_0}=C^{L_0M_0}_{1\mu1\mu'}Y^*_{1\mu}(\boldsymbol{\epsilon})Y_{1\mu'}(\boldsymbol{\epsilon}^*). \quad (20)$$

After long but straightforward application of angular-momentum algebra, one obtains a tensor formulation for the cross section:

$$\frac{d^2\sigma}{d\mathbf{k}_ad\mathbf{k}_p}(l_c,j_c,l_1,l_2,L,S,J)=\alpha\hbar\omega L_\Gamma\sum_{L_0M_0l_al_a''l_pl_p''L_1M_1L_2M_2}(-1)^{M_2}C^{L_0M_0}_{L_1M_1L_2-M_2}\rho^*_{L_0M_0}$$
$$\times[B^i_{l_p}(\mathbf{k}_p)\otimes B^i_{l_a}(\mathbf{k}_a)]_{L_1M_1}[B^{i*}_{l_p''}(\mathbf{k}_p)\otimes B^{i*}_{l_a''}(\mathbf{k}_a)]_{L_2M_2}A^{l_pl_p''l_al_a''}_{L_1L_2L_0}. \quad (21)$$

Equation (21) represents the cross section for Auger-photoelectron emission from solids and is equivalent to Eq. (16). The cross section is given by product of the radiation tensor: the two bipolar scattering amplitudes, which together couple to the rank of the radiation tensor, and the dynamical part $A^{l_p l_p'' l_a l_a''}_{L_1 L_2 L_0}$, which contains combinations of Clebsch-Gordan, 6-j and 9-j coefficients, dipole and Coulomb matrix elements, and is given by:

$$
\begin{aligned}
A^{l_p l_p'' l_a l_a''}_{L_1 L_2 L_0} &= (-1)^{J+L} \hat{j}_c^2 \hat{j}_c^2 \hat{J}^2 \hat{S}^2 \hat{L}^2 \hat{l}_c^2 \hat{l}_c^2 \hat{l}_1^2 \hat{l}_2^2 e^4 \frac{e^4 k_a k_p}{96\pi^3} \\
&\times \sum_{\mu\mu' l_a l_a'' l_p l_p'' k k'} Y^*_{1\mu}(\hat{\epsilon}) Y_{1\mu'}(\hat{\epsilon}^*) R(n_c l_c, E l_p) R^*(n_c l_c, E l_p'') C^{l_p 0}_{l_c 010} C^{l_a'' 0}_{l_c 010} [D_k(n_1 l_1 n_2 l_2, \epsilon l_a n_c l_c) d_{k l_a} \\
&+ (-1)^{-L-S} E_k(n_2 l_2 n_1 l_1, \epsilon l_a n_c l_c) e_{k l_a}] [D^*_{k'}(n_1 l_1 n_2 l_2, \epsilon l_a'' n_c l_c) d_{k' l_a''} + (-1)^{-L-S} E^*_{k'}(n_2 l_2 n_1 l_1, \epsilon l_a'' n_c l_c) e_{k' l_a''}] \\
&\times \sum_{cgfprL_e} (-1)^{-p+g+r-L_2+L_e-L_0} \hat{g}^2 \hat{f}^2 \hat{p}^2 \hat{c}^2 \hat{r}^2 \hat{L}_e^2 \hat{L}_1 \hat{L}_2 \begin{Bmatrix} \frac{1}{2} & \frac{1}{2} & g \\ c & f & \frac{1}{2} \end{Bmatrix} \begin{Bmatrix} l_c & l_c & c \\ \frac{1}{2} & \frac{1}{2} & j_c \end{Bmatrix} \begin{Bmatrix} l_c & l_c & g \\ \frac{1}{2} & \frac{1}{2} & j_c \end{Bmatrix} \begin{Bmatrix} S & S & f \\ \frac{1}{2} & \frac{1}{2} & \frac{1}{2} \end{Bmatrix} \begin{Bmatrix} L & L & f \\ S & S & J \end{Bmatrix} \\
&\times \begin{Bmatrix} L & 1 & p \\ l_c & l_c & c \\ l_a & l_p & L_1 \end{Bmatrix} \begin{Bmatrix} L & 1 & r \\ l_c & l_c & g \\ l_a'' & l_p'' & L_2 \end{Bmatrix} \begin{Bmatrix} 1 & 1 & L_0 \\ L & L & f \\ r & p & L_e \end{Bmatrix} \begin{Bmatrix} r & p & L_e \\ g & c & f \\ L_2 & L_1 & L_0 \end{Bmatrix}. \qquad (22)
\end{aligned}
$$

It is worthwhile to note at this stage that the bipolar scattering amplitude [Eq. (19)] leads to a nonlocal correlation in Eq. (21) between the Auger and the photoelectron amplitudes along their direction of detection, respectively, $\mathbf{k}_a$ and $\mathbf{k}_p$. Such a form of entanglement is however different from the one obtained in the atomic limit [see Eq. (27) below], that was used to describe AR-APECS in Ref. 4. In fact, the entangled form for the photoelectron and the Auger wave functions of Eq. (27) is determined by the bipolar spherical harmonics whose quantum labels (l_{pp}, m_{pp}) and (l_{aa}, m_{aa}) can be directly related to the corresponding atomic labels.[4] On the contrary, the quantum labels of the bipolar scattering amplitude [Eq. (19)] are determined [through Eq. (6)] by all diffraction processes around neighbor atoms, thereby masking the direct atomic-orbital information. The latter, although always present in principle, might therefore be hidden by the multiple scattering in the extended system, as we shall see in Sec. VI.

IV. COINCIDENCE MULTIPLE SCATTERING CROSS SECTION IN THE ATOMIC LIMIT

If we neglect multiple-scattering effects, i.e., the propagator $G^{ij}_{lm,l'm'}$ in Eq. (5), the scattering path operator reduces to its atomic part:

$$
\tau^{ij}_{lml'm'} \rightarrow (t^i_l) \delta_{ll'} \delta_{mm'} \delta_{ij}. \qquad (23)
$$

The atomic scattering matrix is given by

$$
t^i_l = -\frac{1}{k} e^{i\delta_l} \sin(\delta_l), \qquad (24)
$$

where δ_l represents the phase shift of the l partial wave induced by atomic potential scattering. Thus the scattering amplitudes for the photoelectron and the Auger electron become

$$
B^i_{l_p m_p}(\mathbf{k}_p) = t_{l_p} i^{l_p} Y_{l_p m_p}(\hat{\mathbf{k}}_p), \qquad (25)
$$

and

$$
B^i_{l_a m_a}(\mathbf{k}_a) = t_{l_a} i^{l_a} Y_{l_a m_a}(\hat{\mathbf{k}}_a). \qquad (26)
$$

In both cases the sum over atomic sites and angular-momentum labels characterizing Eq. (6) disappears, and, as noted at the end of the previous section and detailed in Ref. 4, the angular-momentum labels are directly related to those of the corresponding core holes. Moreover, in the atomic case, the two bipolar spherical harmonics can be further recoupled and the coincidence cross section can be rewritten as

$$
\begin{aligned}
\frac{d^2\sigma}{d\mathbf{k}_a d\mathbf{k}_p} &= 4\pi^2 \alpha \hbar \omega L_\Gamma \sum_{L_0 M_0 l_{pp} l_{aa}} \rho^*_{L_0 M_0} \\
&\times [Y_{l_{pp}}(\hat{\mathbf{k}}_p) \otimes Y_{l_{aa}}(\hat{\mathbf{k}}_a)]_{L_0 M_0} A^{L_0}_{l_{pp} l_{aa}}. \qquad (27)
\end{aligned}
$$

The dynamical part $A^{L_0}_{l_{pp} l_{aa}}$ differs from Eq. (22) by some angular factors that arise from the coupling of the two bipolar spherical harmonics (see Ref. 4). The angular momenta l_{pp} and l_{aa} are given, respectively, by vector coupling of the photoelectron angular momenta l_p and l_p', and the Auger angular momenta l_a and l_a' (derived from the transition matrix element and its complex conjugate). Both l_{pp} and l_{aa} are restricted to even values due to parity conservation. Generalizing this result to the case where the light polarization properties are expressed by Stokes parameters, one recovers the result given by the statistical-tensor approach for closed-shell systems.[2,3] The application of Eq. (27) to the atomic AR-APECS has been analyzed in Ref. 4.

V. NUMERICAL CALCULATIONS

The numerical calculations have been performed in the case of Ge(100) $L_3M_{45}M_{45}$ Auger-photoelectron coincidence in order to test our theoretical framework against the experimental data of Ref. 11. Radial bound-state wave functions have been calculated using a single configuration Dirac-Fock implementation of Desclaux's program,[15,16] where every state function is given by a Slater determinant of the Dirac orbitals.[17] Such bound-state wave functions are obtained by integration of the Dirac equation using a self-consistent procedure. The code includes the Breit interaction only as a first-order perturbative correction of the self-consistent solution obtained with the Coulomb interaction term only. The muffin-tin approximation has been used to describe the cluster potential even though better approaches have become available recently.[18] The reason is that here we only deal with localized bound states or high-energy continuum states, whose dependence on the detailed shape of the potential is weak. For the final state, the complex Hedin-Lundqvist exchange has been used.[19–21]

In order to perform the numerical calculation of the cross section, we have implemented the coincidence formulas [Eqs. (16) and (21)] in the MS-SPEC package developed by D. Sébilleau.[22] The input variables to be specified in the code are the cluster parameters and the experimental geometry. Several approximations can be used to speed up the calculation: for example, the Rehr-Albers approach[23] is available, which allows a gain in efficiency, with no loss of accuracy in the high-energy regime (as in the present case). This approach takes advantage of the separability of the matrix elements of the photoelectron propagator to reorganize the equations in a plane-wave-like manner with scattering matrices replacing the scalar plane-wave scattering factor. In this way we can get rid of several sums over the angular momenta indices in the MS expansion. Scattering order $N=3$ was used in the calculations. In principle, for coincidence calculations, we implemented both Eqs. (16) and (21). However, whereas Eq. (21) is more transparent from the physical point of view since it separates the dynamics of the process from its geometry, it contains several $6j$ and $9j$ symbols whose calculation strongly increases the CPU time (more than a factor of ten). Thus, only Eq. (16) has been used in the calculations presented in this paper. Such calculations have been performed using a cluster with 2×1 reconstructed surface, as it is known to be the case in Ge.[24]

Before discussing the results, we linger on some approximations used in the analytical derivation of the cross section. The first is the identification of the intermediate state with the quantum numbers of the core hole. As the $2p$ binding energies of Ge occur at 1217.0 $(2p_{3/2})$ and 1248.1 eV $(2p_{1/2})$,[25] their energy separation is sufficient to identify the intermediate ion with such quantum numbers since the spin-orbit coupling is much stronger than the Coulomb interaction between core and valence shells. Moreover, due to this large value of the spin-orbit splitting, the Auger decays related to these spin-orbit-partner edges do not overlap and the Auger spectra related to only one of the two holes can be studied without any ambiguity. Finally, for what the final states of the Auger decay are concerned, we consider them as labeled by the two final holes without considering further recoupling of the latter with any other open shell. This simplified description seems to be appropriate for the case of the $L_3M_{45}M_{45}$ spectrum in Ge, which shows distinct structures related to the multiplet terms obtained by just coupling the two holes.[26]

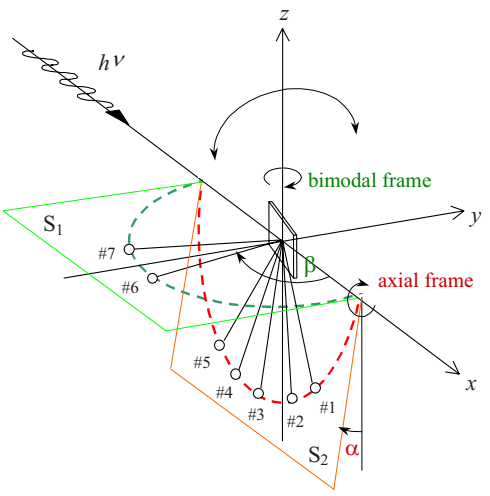

FIG. 1. (Color online) The experimental setup of Ref. 11.

The transition can be schematized as

$$h\nu + Ge \rightarrow Ge^{+}2p_{3/2}^{-1} + e_p^{-}(\epsilon_s, \epsilon_d) \rightarrow Ge^{2+}3d^8(^1G_4) + e_a^{-}(\epsilon_f, \epsilon_h). \tag{28}$$

The kinetic energies of the photoelectron and of the Auger electron are 250 and 1139 eV, respectively.[11] Of the whole multiplet structure originated by the $L_3M_{45}M_{45}$ process in Ge, only the $^1G_4$ term (the most intense) is considered in our calculations, as the authors of Ref. 11 were able to resolve the different terms.

VI. RESULTS

All the details of the experiment that we want to describe are reported in Ref. 11 and only a brief description is given here. A monochromatized beam ($\hbar\omega=1472$ eV) of linearly polarized photons, nearly p polarized, impinges at a grazing angle of 6° onto a Ge(100) single-crystal surface with the 2×1 reconstruction. Seven electron analyzers were arranged in two independent rotatable frames, as depicted in Fig. 1. Due to the grazing angle, the surface normal in this figure corresponds to $\beta=96°$ and not $\beta=90°$. The five analyzers 1–5 in Fig. 1, placed at intervals of 18° on the axial frame (which is fixed in this experiment), were tuned to monitor the Ge $2p_{3/2}$ photoelectron in a plane that contained the photon beam propagation direction and was rotated 54° from the sample normal (i.e., the α angle in Fig. 1 is 36°). One of the axial analyzer (analyzer 3 in Fig. 1) was in the plane perpendicular to the photon beam propagation direction at 54° from the polarization vector while the others were symmetric with respect to this plane. In order to scan the Auger-electron-diffraction (AED) pattern, the two analyzers on the bimodal

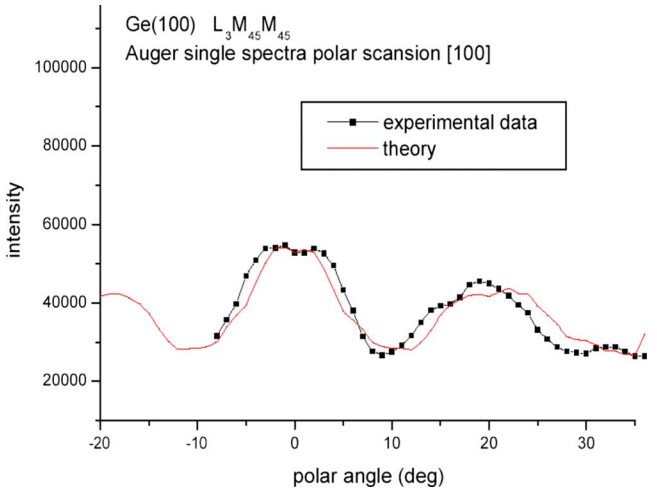

FIG. 2. (Color online) Theoretical curve for Ge(100) $L_3M_{45}M_{45}$ AED and comparison with the experimental data from Ref. 11.

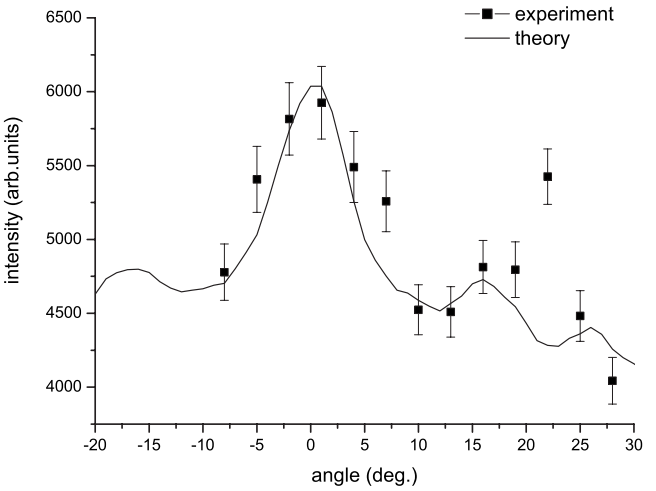

FIG. 3. Theoretical curve for Ge(100) $L_3M_{45}M_{45}$ APECS (summed over the five photoelectron directions) and comparison with the experimental data from Ref. 11.

frame (6 and 7 in Fig. 1), placed in the plane containing both the polarization and the propagation direction of the photon beam, were rotated to monitor the Ge(100) $L_3M_{45}M_{45}$ ($^1G_4$) Auger-electron emission intensity as a function of the polar angle. This scan gave rise both to the single AED pattern and to the coincidence pattern with the latter recorded in coincidence with five different values of the photoelectron wave vector, selected by the five axial analyzers. The conventional AED pattern and the coincidence patterns were recorded simultaneously.

A. Auger diffraction

In Fig. 2 we present our calculations for the Auger diffraction pattern and compare it with the experimental data from Ref. 11. The theoretical calculations succeed in reproducing the main structures, i.e., the main peak along the normal to the surface at 0° and the feature at 20°. The latter is shifted by ~2° with respect to experimental data, probably due to an underestimation of the internal potential. However, it's splitting into two subpeaks and their relative intensities are correctly reproduced in the calculation. The anisotropy of the data is overall well described and also the double peak structure at 0° is present in the theoretical *ab initio* analysis. As it was already suggested in Ref. 11, the double structure appears because of emission from the deepest layers. Indeed, the calculation shown in Fig. 2 is obtained by summing up all signals of the upper nine atomic planes. The origin of such features was reported even for other materials, such as MgO, as originating from deeper linear atomic chains not parallel to the surface normal.[27]

B. Coincidence results

The comparison between the coincidence calculation summed over the five different directions of the photoelectron and the corresponding experimental data is shown in Fig. 3. The main peak at 0° is correctly reproduced, and there is a fair overall agreement between theory and experiment except for a single experimental point at 22°.

We stress that coincidence calculations converge to the curve shown in Fig. 3 within seven atomic planes, compared to the nine atomic planes for the conventional AED shown in Fig. 2, which indicates the enhanced surface sensitivity of the technique. For the same reason, the double peak structure around 0°, which is present in the AED conventional pattern, disappears in the coincidence theoretical curve, being determined, as sketched above, by interference effects with electron paths coming from deeper layers.

The theoretical curves obtained for the coincidence Auger diffraction data are shown in Fig. 4. The principal discrepancy of our calculations with the experimental data is determined by the theoretical pinning of the main peak at 0°, whereas the experimental coincidences show a shift of this peak in all spectra. Since such a displacement was one of key arguments in Ref. 11 in assuming the sensitivity of the technique to atomic alignment even in solid state, it is worthwhile to linger on this subject with a more detailed analysis.

In the atomic case, the atomic-orbital sensitivity of the coincidence spectroscopy has been demonstrated within the multiple-scattering approach in Ref. 4. We remind that the reason for such sensitivity is determined by the variation in the intermediate-ion alignment, which, in turn, was implied by the different direction of detection of the photoelectron. This causes nonuniform distribution of the m_l sublevels in Auger source wave, which leads to the angular shifts in the Auger scan. Here we want to test the idea that such sensitivity to atomic alignment can survive diffraction effects of a solid sample and even be amplified along peculiar directions by the well-known forward-focusing effect. In this framework, an initial nonstatistical distribution in the source wave of the Auger electron would imply different shapes in the coincidence diffraction spectra, compared to the conventional Auger. In principle, such an idea is well defined: multiple-scattering calculations performed for an electron ejected from the Ge(100) surface with an energy between 250 and 1150 eV have demonstrated that the main peak along the normal is almost entirely determined by the $m_l = 0$ source wave, enhanced by the forward focusing along the

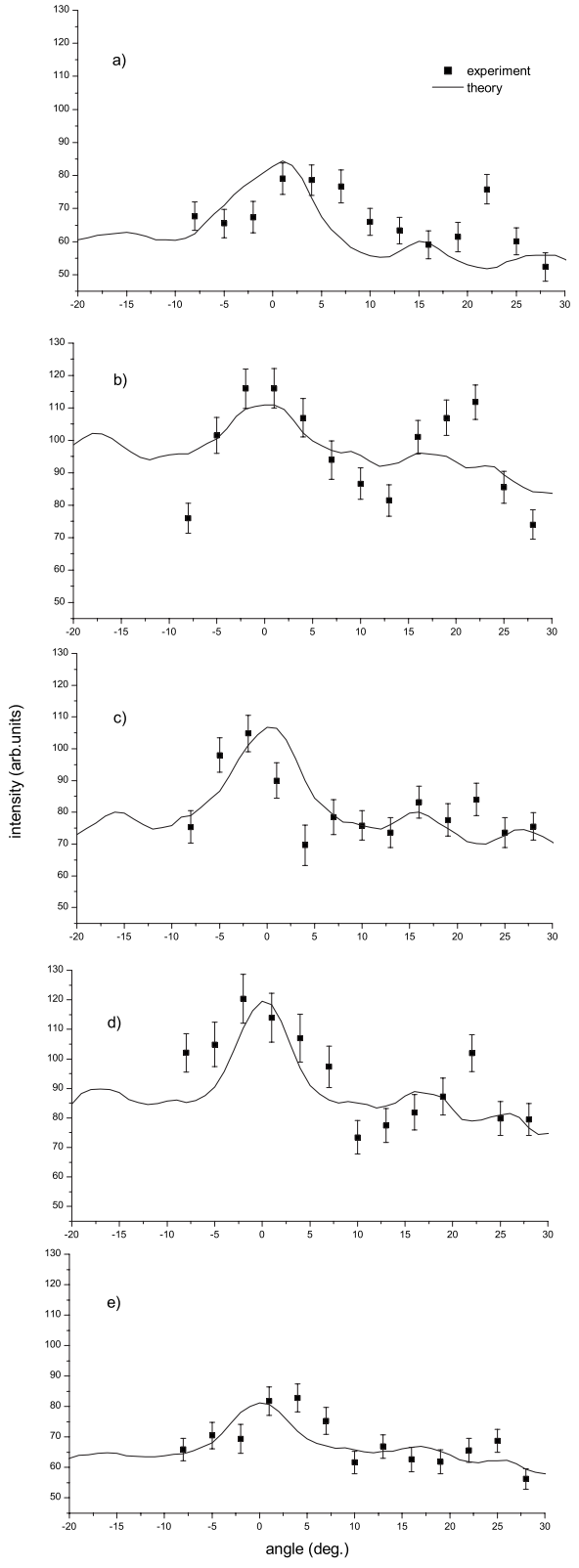

FIG. 4. APECS theoretical results corresponding to the five different directions of the photoelectron for Ge(100) $L_3M_{45}M_{45}$ [(a) photoelectron detected by analyzer 1, (b) by analyzer 2, (c) by analyzer 3, (d) by analyzer 4, and (e) by analyzer 5] and comparison with the experimental data from Ref. 11.

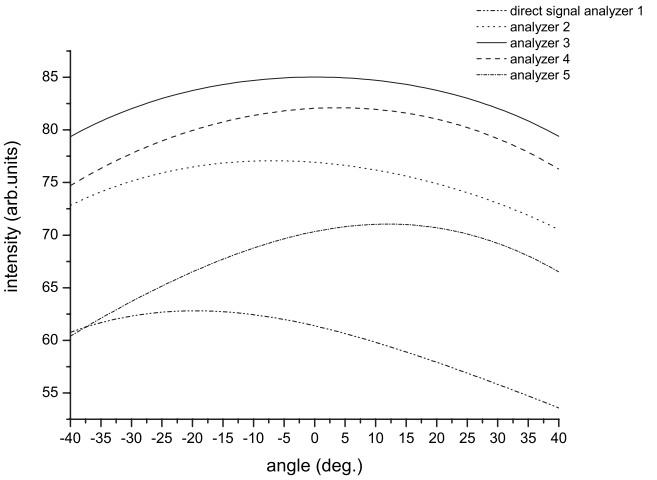

FIG. 5. Ge(100) $L_3M_{45}M_{45}$ APECS direct signals corresponding to the five different directions of the photoelectron.

normal. Therefore, an initial $m_l=0$ anisotropy in the Auger source wave would have led to a spectrum entirely peaked along the normal, thereby immediately confirming such a selectivity. However, our calculations also show that when the photoelectron is not detected along the normal, several m_l contribute in such a way that the source wave is much less polarized and an eventual alignment contribution in the coincidence spectrum is necessarily hidden by other solid-state contributions. These qualitative considerations can be substantiated by the following arguments, driving us to the conclusion that in the geometrical conditions of Ref. 11. the differences in the experimental shapes of coincidence spectra are not determined by the orbital selectivity due to the alignment of the intermediate ion.

In order to check the sensitivity to alignment that characterizes APECS in the atomic case, we have plotted in Fig. 5 the "direct signal," i.e., the coincidence spectrum before the Auger and the photoelectron are allowed to diffract. Such a signal should mimic the atomic case. Interestingly, in this case, a shift of the peaks around 0° is present: whereas the coincidence signal with analyzer 3 keeps the axial symmetry about the normal, the other four coincidence signals are all displaced. However, there is an important difference compared to the experimental shifts, which are all in the same directions for the pairwise symmetric analyzers (respectively, 1 and 5, and 2 and 4): the theoretical shifts are characterized by an opposite behavior, positive for analyzers 4 and 5, and negative for analyzers 1 and 2. The same behavior, opposite Auger shift corresponding to opposite photoelectron detectors with respect to 0°, was also found in the atomic case in Ref. 4. This evidence prevents the explanation of the observed peak displacement on the basis of the degree of alignment of the source waves.

During the diffraction process, the wave is allowed to change its (l,m_l) quantum numbers due to the loss of spherical symmetry. We have plotted in Fig. 6 the evolution of the diffracted signal when the scattering processes from the different planes are taken into account. We only showed the angular pattern of Auger electrons in coincidence with photoelectrons detected at analyzer 5 but the general behavior is

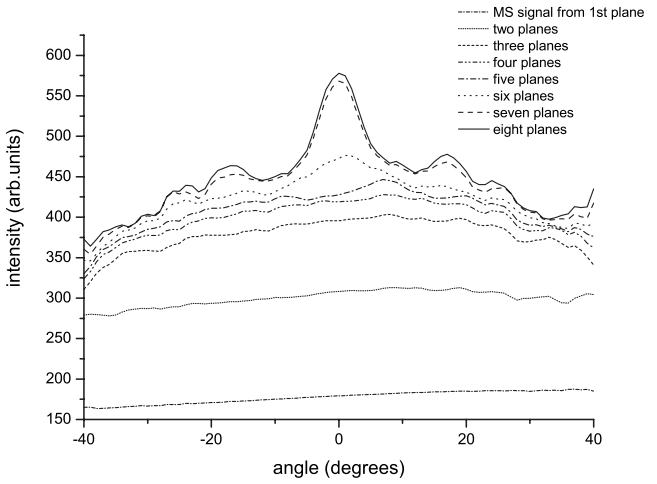

FIG. 6. Auger angular scan in coincidence with the photoelectron detected at analyzer 5, originating at different planes, in order to highlight the formation of the diffraction pattern.

unaltered for the other four coincidence signals with the main peak always pinned at 0°. What can be deduced from these calculations is the following: even though the direct signal of analyzer 5 is asymmetric with respect to 0°, its asymmetry is too small to give rise to an asymmetric peak in the diffracted signal around 0°. Such an asymmetry could have been detected only in a much wider angular region than the experimentally measured $[-10°, +30°]$. For example, the signal at +40°, in coincidence with analyzer 5, is more intense than the signal at −40°: the opposite is true for the Auger coincidences with analyzer 1. However, the peak around 0° is basically insensitive to the atomic anisotropy.

Moreover, the theoretical curve corresponding to Auger diffraction, in coincidence with photoelectrons detected by analyzer 3, is almost perfectly symmetric with respect to the 0° direction (the normal to the surface). On the contrary, small asymmetries are evident for analyzers 1, 2, 4, and 5. Such asymmetries could have been qualitatively expected because the plane perpendicular to the photon beam, with respect to these 4 analyzers, which are pairwise symmetric, is not a symmetry plane for the 2×1 reconstructed surface due to the different directions of the dimerized bonds. Indeed we found that coincidence *ab initio* calculations are quite sensitive to the details of the reconstructed surface. The presence of such structural surface effects might have therefore played a bigger role on the coincidence spectrum than on AED due to the greater sensitivity to the surface.

Finally, although we are unable to identify the origin of the experimental displacement of the coincidence peak at 0°, our calculations suggest that the small alignment of the intermediate ion is, in the present case, completely obscured by solid-state effects, and that APECS might not be sensitive to atomic-orbital correlations in the angular region and at the energies studied in Ref. 11.

VII. CONCLUSIONS

In this work we have derived the differential cross section for Auger-photoelectron coincidence spectroscopy in condensed matter. Such a cross section can be written as a product of a dynamical part, the radiation tensor, and a structural part given by the coupled scattering amplitudes of the two outgoing electrons. The angular correlations of the two electrons in this approach arise only at the atomic level through the transition selection rules imposing that the Auger decay fills in the orbital level whose quantum numbers characterize also the state of the emitted photoelectron. In the limiting case of atomic emission, our formalism correctly matches the well-known statistical-tensor approach for closed-shell atoms.[4]

Numerical calculations both for conventional AED and coincidence patterns have been performed for the case of Ge(100) $L_3M_{45}M_{45}$. Our theoretical results indicate that: (i) the APECS signal, as expected, is more sensitive to the surface than the Auger signal and, in particular, to the reconstruction. (ii) On the basis of Eq. (16), atomic-orbital information (i.e., the alignment of the intermediate ion) could be, in principle, extracted, as predicted in Ref. 11. (iii) However, in the analyzed geometrical conditions and energy region ($E_A\sim1139$ eV and $E_P\sim250$ eV), multiple-scattering effects enhanced by forward focusing nearly completely swamp the atomic information, as shown in Fig. 6.

In spite of the results obtained in the specific energy and angular regions studied in this paper, it seems to us interesting that point (ii) leaves the door open to the possible detection of the effect predicted in Ref. 11. In order to perform a key experiment to demonstrate that the diffraction coincidence patterns keep a more noticeable memory of the initial atomic-orbital correlation, we suggest choosing a geometry such that at least one photoelectron detector is placed along the surface normal and that the Auger detectors could also move as close as possible to this same direction. Clearly, these speculations need a deeper theoretical analysis of the optimal energy range for the photoelectron detection, which will be addressed in future investigations.

ACKNOWLEDGMENTS

Financial support from the MIUR PRIN 2005 contract "Studio di sistemi ad alta correlazione e bassa dimensionalita' con spettroscopie di coincidenza: una nuova generazione di metodi sperimentali e teorici" and from INFM program "Supporto utenti luce di sincrotrone" is gratefully acknowledged.

[1] R. A. Bartynski, A. K. See, W.-K. Siu, and S. L. Hulbert, in *Correlation Spectroscopy of Surfaces, Thin Films, and Nanostructures*, edited by J. Berakdar and J. Kirschner (Wiley, New York, 2004).
[2] N. M. Kabachnik, J. Phys. B **25**, L389 (1992).
[3] V. V. Balashov, A. N. Grum-Grzhimailo, and N. M. Kabachnik, *Polarization and Correlation Phenomena in Atomic Collisions* (Kluwer, Dordrecht/Plenum, New York, 2000).
[4] F. Da Pieve, S. Di Matteo, D. Sébilleau, R. Gunnella, G. Stefani, and C. R. Natoli, Phys. Rev. A **75**, 052704 (2007).
[5] P. Bolognesi, A. De Fanis, M. Coreno, and L. Avaldi, Phys. Rev. A **70**, 022701 (2004).
[6] R. Hentges, N. Müller, J. Viefhaus, U. Heinzmann, and U. Becker, J. Phys. B **37**, L267 (2004).
[7] The effective inelastic mean-free path is given by $\lambda_c \equiv \lambda_p\lambda_a/(\lambda_p+\lambda_a) < \lambda_p, \lambda_a$, where λ_p and λ_a are the inelastic mean-free path for the photoelectron and the Auger electron, respectively.
[8] R. A. Bartynski, S. Yang, S. L. Hulbert, C.-C. Kao, M. Weinert, and D. M. Zehner, Phys. Rev. Lett. **68**, 2247 (1992).
[9] W. S. M. Werner, W. Smekal, H. Störi, H. Winter, G. Stefani, A. Ruocco, F. Offi, R. Gotter, A. Morgante, and F. Tommasini, Phys. Rev. Lett. **94**, 038302 (2005).
[10] A. Liscio, R. Gotter, A. Ruocco, S. Iacobucci, A. G. Danese, R. A. Bartynski, and G. Stefani, J. Electron Spectrosc. Relat. Phenom. **137-140**, 505 (2004).
[11] R. Gotter, A. Ruocco, M. T. Butterfield, S. Iacobucci, G. Stefani, and R. A. Bartynski, Phys. Rev. B **67**, 033303 (2003).
[12] D. Sébilleau, R. Gunnella, Z. Wu, S. Di Matteo, and C. R. Natoli, J. Phys.: Condens. Matter **18**, R175 (2006).
[13] C. R. Natoli, M. Benfatto, C. Brouder, M. F. Ruiz López, and D. L. Foulis, Phys. Rev. B **42**, 1944 (1990).
[14] D. A. Varshalovich, A. N. Moskalev, and V. K. Khersonskii, *Quantum Theory of Angular Momentum* (World Scientific, Singapore, 1996), p. 144, Eqs. (9) and (14).
[15] J. P. Desclaux, Comput. Phys. Commun. **9**, 31 (1975).
[16] A. L. Ankudinov, S. I. Zabinsky, and J. J. Rehr, Comput. Phys. Commun. **98**, 359 (1996).
[17] W. R. Johnson and K. T. Cheng, in *Atomic Inner Shell Physics*, edited by Bernd Crasemann (Plenum, New York, 1985), Chap. 1, pp. 1–29.
[18] K. Hatada, K. Hayakawa, M. Benfatto, and C. R. Natoli, Phys. Rev. B **76**, 060102(R) (2007).
[19] K. H. Johnson, Adv. Quantum Chem. **7**, 143 (1973).
[20] T. A. Tyson, K. O. Hodgson, C. R. Natoli, and M. Benfatto, Phys. Rev. B **46**, 5997 (1992).
[21] S.-H. Chou, J. J. Rehr, E. A. Stern, and E. R. Davidson, Phys. Rev. B **35**, 2604 (1987).
[22] MS-SPEC code by D. Sébilleau (multiple-scattering code for photoelectron, Auger-electron diffraction, APECS, EXAFS, and LEED). Available upon request (didier.sebilleau@univ-rennes1.fr).
[23] J. J. Rehr and R. C. Albers, Phys. Rev. B **41**, 8139 (1990).
[24] R. M. Tromp, R. J. Hamers, and J. E. Demuth, Phys. Rev. Lett. **55**, 1303 (1985).
[25] *Photoemission in Solids*, edited by L. Ley and M. Cardona (Springer, Berlin, 1979), Vol. II.
[26] E. Antonides, E. C. Janse, and G. A. Sawatzky, Phys. Rev. B **15**, 1669 (1977).
[27] D. Agliz, A. Quémerais, and D. Sébilleau, Surf. Sci. **343**, 80 (1995).